

1 Article

# 2 Modeling dislocation contrasts obtained by 3 accurate-Electron Channeling Contrast Imaging for 4 characterizing deformation mechanisms in bulk 5 materials

6 Hana KRIAA <sup>1</sup>, Antoine GUITTON <sup>1,2</sup> and Nabila MALOUFI <sup>1,2,\*</sup>

7 <sup>1</sup> Université de Lorraine - CNRS - Arts et Métiers ParisTech – LEM3, 7 rue Félix Savart, 57070 Metz, France;  
8 hana.kriaa@univ-lorraine.fr (H.K.); antoine.guitton@univ-lorraine.fr (A.G.); nabila.maloufi@univ-lorraine.fr  
9 (N.M.)

10 <sup>2</sup> Laboratory of Excellence on Design of Alloy Metals for low-mAss Structures (DAMAS) – Université de  
11 Lorraine, 57073 Metz, France.

12 \* Correspondence: nabila.maloufi@univ-lorraine.fr; Tel.: +33 372 747 865

13 Received: date; Accepted: date; Published: date

14 **Abstract:** Electron Channeling Contrast Imaging (ECCI) is becoming a powerful tool in Materials  
15 Science such as for characterizing deformation defects. Dislocations observed by ECCI in Scanning  
16 Electron Microscope, exhibit several features depending on the crystal orientation relative to the  
17 incident beam (white/black line on a dark/bright background). In order to bring new insights  
18 concerning these contrasts, we report an original theoretical approach based on the dynamical  
19 diffraction theory. Our calculations led, for the first time, to an explicit formulation of the  
20 backscattered intensity as function of various physical and practical parameters governing the  
21 experiment. Intensity profiles are modeled for dislocations parallel to the sample surface for  
22 different channeling conditions. All theoretical predictions are consistent with experimental  
23 results.

24 **Keywords:** ECCI, dislocation contrast, modeled intensity profiles, invisibility criteria, dynamical  
25 theory of electron diffraction.  
26

---

## 27 1. Introduction

28 The Electron Channeling Contrast Imaging (ECCI) takes advantage from the strong dependency of  
29 the BackScattered Electrons (BSE) signal on the orientation of the incident beam with the lattice  
30 planes due to the electron channeling mechanism [1]. Therefore, any slight local distortion of the  
31 crystal lattice, produced for instance by a dislocation leads to a BSE intensity ( $I_{BSE}$ ) modulation, thus  
32 generating several contrasts such as bright line on a dark background [2] or black line on bright  
33 background [3].

34 For understanding the origin of the dislocation contrasts obtained by ECCI, the two-beam dynamical  
35 diffraction theory was adapted from the Transmission Electron Microscopy (TEM) [4] [5]. Briefly, the  
36 electron beams are described, inside the crystal, by a superposition of Bloch waves. The different  
37 inelastic scattering events are divided into two categories: those scattered through angles less than  
38  $90^\circ$  (forming the forward scattering wave) and those scattered through angles greater than  $90^\circ$   
39 (forming the backscattered wave) [6]. In the multiple scattering model electrons can be removed  
40 from the forward scattering wave to the backscattered one and vice-versa. In order to simulate the  
41  $I_{BSE}$  profiles for both perfect and imperfect crystal, Spencer *et al.* [7] and Wilkinson *et al.* [6, 8, 9] used  
42 this Bloch wave-based model. They showed that for the perfect crystal, the simulated profiles exhibit

43 the main experimental features of the channeling pattern: bright band and dark edges. The same  
 44 approach was also used by Reimer [10, 11] for a perfect crystal where the multiple scatterings are  
 45 treated as incoherent. These different approaches, were extended to the case of an imperfect crystal  
 46 containing a dislocation [6-9] or a stacking fault [12]. Despite their contribution to the theory of the  
 47 defects electron channeling contrasts [7-12], detailed calculations leading to an analytical expression  
 48 of BSE signal as a function of experimental parameters, is still missing. Furthermore, in most cases  
 49 [7,8] theoretical results were not confronted with the experiments. This can be illustrated from the  
 50 dislocation profiles calculated for Bragg condition, which exhibit an extra-pic of  $I_{BSE}$  not observed  
 51 experimentally [7, 8].

52 To go deeper in the understanding of the observed channeling contrast of dislocations, we propose  
 53 an easier way for modeling the  $I_{BSE}$  as a function of physical parameters either relative to the material  
 54 or governing the ECCI experiment. Our theoretical results show a good agreement with the  
 55 experiments for several diffraction conditions.

56 In a crystal, the electronic wave function is solution of the time independent Schrödinger's equation  
 57 and is given by [11]:

$$58 \quad \Psi(\mathbf{r}) = \sum_j \varepsilon^{(j)} \sum_g C_g^{(j)} e^{[2\pi i (\mathbf{k}_0^{(j)} + \mathbf{g}) \cdot \mathbf{r}]} e^{[-2\pi q^{(j)} z]} \quad (1)$$

59 The index  $j$  refers to the  $j$ th wave,  $\varepsilon^{(j)}$  are the excitation amplitudes of the Bloch wave  $\psi^{(j)}$ ,  $C_g^{(j)}$  are  
 60 the amplitudes of the diffracted waves with a wave vector  $\mathbf{k}_g^{(j)} = \mathbf{k}_0^{(j)} + \mathbf{g}$ , where  $\mathbf{k}_0^{(j)}$  is the wave vector  
 61 of the  $j$ th primary wave and  $\mathbf{g}$  is the diffraction vector.  $\mathbf{r}$  is the spatial position vector at which the  
 62 electron intensity is evaluated. The second factor of equation (1) contains the absorption parameter  
 63  $q^{(j)}$  expressing the exponential attenuation of the wave amplitude with increasing depth  $z$ .  
 64

65 In order to determine the different coefficient of the Bloch wave function, presented in equation (1),  
 66 Reimer used the two-beam condition *i.e.* only one set of lattice planes are in channeling condition.  
 67 Hence, the total BSE signal of a slice of a thickness  $dz$ , located at a depth  $z$  is given by [11]:

$$68 \quad \frac{d\eta}{dz} = N\sigma_B \{ \psi\psi^* + (1 - \sum_j |C_0^{(j)}|^2 e^{[-4\pi q^{(j)} z]} ) \} \quad (2)$$

69  $N$  is the atom number per unit of volume,  $\sigma_B$  is the backscattering cross-section through angles  
 70 larger than  $90^\circ$  and  $\psi\psi^*$  is the probability for the Bloch wave to be backscattered at a depth  $z$ . The  
 71 last terms (in parentheses) in equation (2) describes the electrons that are removed from the Bloch  
 72 wave field by scattering before reaching the slice  $dz$ .  
 73

74 The BSE coefficient  $\eta_{o.c.}$  is, then, obtained from the integration of equation (2) in the total interaction  
 75 depth from  $z=0$  to  $z \rightarrow \infty$  (labelled  $\Delta\eta$  in Reimer's model). O.C. indicates that only the total BSE  
 76 intensity due to orientation contrast is calculated, while the contributions due to atomic number and  
 77 to the surface inclination are not considered [11]:

$$\eta_{0.c.} = \frac{N\sigma_B}{4\pi} \xi_0' \left( -\frac{s \xi_g + \frac{\xi_0}{\xi_g}}{1+(s \xi_g)^2 - \left(\frac{\xi_0}{\xi_g}\right)^2} + \frac{\omega}{1+(s \xi_g)^2 + [(1+(s \xi_g)^2)\left(\frac{\xi_0}{\xi_g}\right)]^2} \right) \quad (3)1$$

Equation (3) corresponds to the variation of the BSE intensity for a perfect crystal i.e. the intensity profile of an isolated pseudo-Kikuchi band [7,11,13]. Some of the parameters of equation (3) will be defined later in the text.

## 2. Our theoretical approach for BSE intensity calculation for an imperfect crystal

If we consider a column located at a position  $x$  away from a dislocation, at a position  $x=0$  and depth  $z=z_D$  (where  $z_D$  is the mean depth of the dislocation), the distortion of the lattice planes nearby the dislocation does not depend on  $z$  but only on  $x$  and it is given by  $\left(\frac{\partial \mathbf{R}}{\partial z}\right)_{z=z_D}$  ( $\mathbf{R}$  is the displacement field of the crystalline planes) [14].

Therefore, for calculating the  $I_{BSE}$  in the case of an imperfect crystal containing a dislocation parallel to the sample surface, independently of the depth  $z$ , we take into account a new deviation parameter  $s'$  written by:

$$s' = s + s_D \quad \text{where} \quad s_D = \mathbf{g} \cdot \left(\frac{\partial \mathbf{R}}{\partial z}\right)_{z=z_D} \quad (4)$$

$s$  is the deviation from the exact Bragg position in the perfect crystal, which can be experimentally measured [3]. The scalar product  $\mathbf{g} \cdot \left(\frac{\partial \mathbf{R}}{\partial z}\right)_{z=z_D}$  represents the supplementary deviation,  $s_D$  due to the variation of the incidence angle between the primary beam and the distorted crystalline planes near the dislocation core. Far from the dislocation, the crystal is considered as perfect. The planes are not distorted and the deviation  $s_D$  becomes zero. Consequently, to take into account the presence of the defect, we substitute  $s$  by  $s'$  in the expression of  $\eta_{0.c.}$  for a perfect crystal (in equation 3, which does not depend on  $z$ ). We obtain:

$$\eta_{0.c.} = \frac{N\sigma_B}{4\pi} \xi_0' \left( -\frac{(s+s_D(x)_{z=z_D})\xi_g + \frac{\xi_0}{\xi_g}}{1+((s+s_D(x)_{z=z_D})\xi_g)^2 - \left(\frac{\xi_0}{\xi_g}\right)^2} + \frac{(s+s_D(x)_{z=z_D})\xi_g}{1+((s+s_D(x)_{z=z_D})\xi_g)^2 + [(1+((s+s_D(x)_{z=z_D})\xi_g)^2)\left(\frac{\xi_0}{\xi_g}\right)]^2} \right) \quad (5)$$

This allow to study the variation of the  $I_{BSE}$  as a function of  $x$  (distance  $x$  away from the dislocation core). Where, the contrast associated to a dislocation is described by  $s_D$  (containing all the effect of  $\mathbf{R}$ ).

### 2.1. Screw dislocation

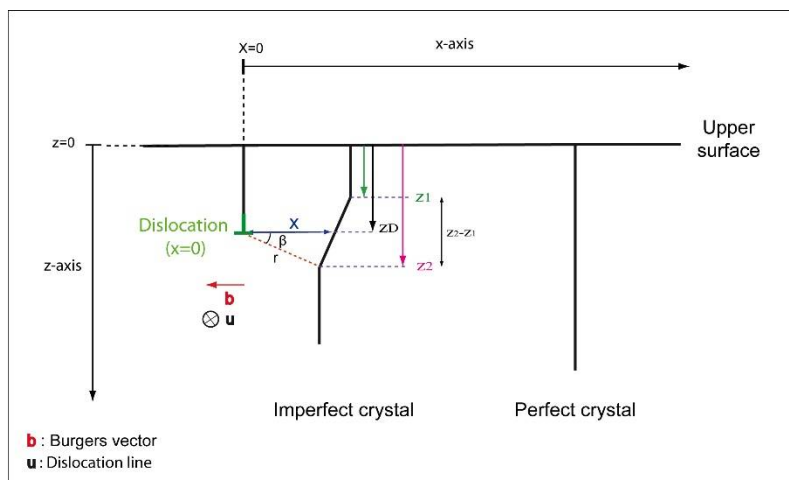
Figure 1 shows a screw dislocation parallel to the surface of a bulk sample and located at a depth  $z_D$ . This defect is characterized by a Burgers vector  $\mathbf{b}$  and a line direction  $\mathbf{u}$ . At a distance  $x$  away from the dislocation core (in  $x=0$ ), the crystal plane is deformed. The displacement field  $\mathbf{R}_{\text{screw}}$  is then defined in polar coordinate ( $\beta$ ) as follows [15]:

---

1 Note that in the book of Reimer [11], equation (3) contains an error: it is written  $2\pi$  to the denominator instead of  $4\pi$ .

$$107 \quad \mathbf{R}_{\text{screw}} = \frac{\mathbf{b}}{2\pi} = \frac{\mathbf{b}}{2\pi} \tan^{-1} \left( \frac{z-z_D}{x} \right) \quad (6)$$

108



109

110

**Figure 1.** Schematic of an edge dislocation parallel to the surface and located at a depth  $z_D$ . Deformed planes, perpendicular to the surface, are at a distance  $x$  away from the dislocation core.

111

112

113 The derivative of  $\mathbf{R}_{\text{screw}}$  with respect to the depth  $z$ , at a turning point ( $z = z_D$ ), is given by:

$$114 \quad \left. \frac{d\mathbf{R}_{\text{screw}}}{dz} \right|_{z=z_D} = \frac{\mathbf{b}}{2\pi x \left( 1 + \left( \frac{z-z_D}{x} \right)^2 \right)} \Bigg|_{z=z_D} = \frac{\mathbf{b}}{2\pi x} \quad (7)$$

115 Based on this reasoning, the substitution of equation (7) in equation (5) allows us to obtain the  
116 following expression of  $\eta_{0.c.}$ :

$$117 \quad \eta_{0.c.} = \frac{N_{OB}}{4\pi} \xi_0' \left( - \frac{\left( s + \frac{\mathbf{g} \cdot \mathbf{b}}{2\pi x} \right) \xi_g + \frac{\xi_0'}{\xi_g}}{1 + \left( \left( s + \frac{\mathbf{g} \cdot \mathbf{b}}{2\pi x} \right) \xi_g \right)^2 - \left( \frac{\xi_0'}{\xi_g} \right)^2} + \frac{\left( s + \frac{\mathbf{g} \cdot \mathbf{b}}{2\pi x} \right) \xi_g}{1 + \left( \left( s + \frac{\mathbf{g} \cdot \mathbf{b}}{2\pi x} \right) \xi_g \right)^2 + \left[ 1 + \left( \left( s + \frac{\mathbf{g} \cdot \mathbf{b}}{2\pi x} \right) \xi_g \right)^2 \left( \frac{\xi_0'}{\xi_g} \right)^2 \right]} \right) \quad (8)$$

118 Equation (8) gives the variation of the BSE signal as a function of the distance  $x$  and the experimental  
119 parameters such as the deviation  $s$  and the diffraction vector  $\mathbf{g}$ .

120 It should be noted that in this paper, we show profiles modeled in the case of aluminum, where the  
121 used parameters are: acceleration voltage  $E=20$  kV,  $\mathbf{g} = (220)$ , the extinction distance  $\xi_g = 50$  nm,

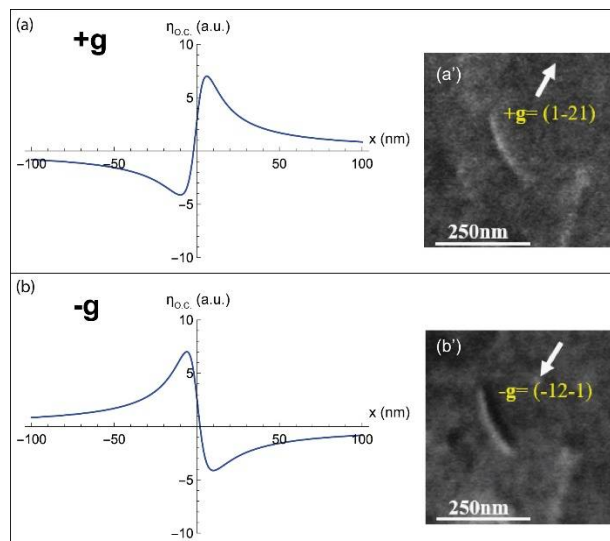
122 absorption lengths  $\xi_0' = 140$  nm and  $\xi_g' = 600$  nm [11]. It should also be mentioned that in all modeled  
123 profiles the background level will be taken as reference (at the zero of the ordinate axis). All negative  
124 values then correspond to lower BSE intensities than the background level.

### 125 2.1.1. Deviation parameter $s=0$

126 The theoretical intensity profiles calculated from equation (8), in the case of a screw dislocation, for  
127 the diffraction conditions  $s=0$  and  $\pm \mathbf{g}$  are represented in Figure 2. Their corresponding  
128 experimental ECC micrographs are also showed (Figures 2a' and b'). The  $\mathbf{g}$  and  $\mathbf{s}$  vectors are,  
129 respectively, determined experimentally through the pseudo-band indexation of the HR-SACP  
130 (High Resolution Selected Area Channeling Pattern) assisted by EBSD experiment [2, 3].

131

132 For both  $+g$  and  $-g$  diffractions, the dislocation profiles (Figures 2.a and b) are anti-symmetric: a  
 133 hollow and a peak corresponding to the black and white sides of the dislocation respectively  
 134 (Figures 2a' and b'). Moreover, in the case of  $-g$ , the extrema are inverted compared to those  
 135 observed for  $+g$ : the peak becomes hollow and vice versa.

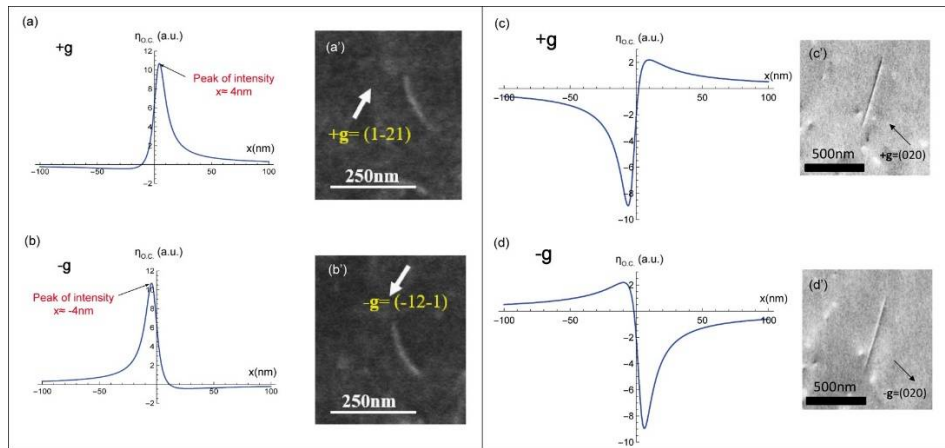


136  
 137 **Figure 2.**  $I_{BSE}$  profiles modeled, for a screw dislocation parallel to the surface, with a deviation parameter  $s=0$   
 138 for the diffractions (a)  $+g$  and (b)  $-g$  with their corresponding experimental ECC micrographs (a') and (b').  
 139

140 Such theoretical results reveals that at Bragg position, a screw dislocation generates a BSE image  
 141 with black/white sides, which reverse with the inversion of the sign of  $g$ . Therefore, equation (8) is in  
 142 good agreement with the experimental observations already reported in literature [3,7].  
 143

#### 144 2.1.2. Deviation parameter $s>0$

145 The  $I_{BSE}$  profiles calculated by equation (8) with a deviation parameter slightly positive ( $s=0.01 \text{ nm}^{-1}$ )  
 146 are represented in Figures 3a and b for the  $+g$  and  $-g$  diffractions respectively. In this condition  
 147 ( $s>0$ ), both  $\pm g$  dislocation profiles present one intensity peak only. This is in agreement with the  
 148 experimental ECC micrographs shown in Figures 3a' and b': bright line on dark background. Note  
 149 also that the maximum intensity does not coincide with the exact position of the dislocation core  
 150 ( $x=0 \text{ nm}$ ) but it is at  $x \approx \pm 4 \text{ nm}$ : it is displaced from one side of the dislocation position to the other  
 151 side when changing from  $+g$  to  $-g$ . Such result is analogous to that obtained in TEM and can be  
 152 used to characterize a dislocation configuration consisting of two parallel dislocations such as dipole  
 153 [3, 16].  
 154



155  
 156 **Figure 3.** I<sub>BSE</sub> profiles modeled, for a screw dislocation parallel to the surface, with  $s>0$  and  $s<0$  for (a) (c)  $+g$   
 157 and (b) (d)  $-g$  with their corresponding experimental ECC micrographs (a'), (b'), (c') and (d').

### 158 2.1.3. Deviation parameter $s<0$

159 The I<sub>BSE</sub> profiles calculated from our theoretical model for a slightly negative deviation parameters  
 160 ( $s=-0.01 \text{ nm}^{-1}$ ) and  $\pm g$  diffraction conditions are represented in Figure . For the diffraction  $+g$ , the  
 161 curve contains a deep hollow and a peak corresponding to the black and white dislocations sides  
 162 respectively (Figure 3c'). This contrast is inverted with the inversion of the sign of  $g$  (Figures 3d and  
 163 d'). For  $s<0$ , the BSE signal emitted from the zone of interest is high: bright background.

### 164 2.2. Edge dislocation

165 Similar to screw dislocation, an edge dislocation parallel to the surface and located at a depth  $z_D$   
 166 produces a local deformation of the crystalline planes nearby its core. Such distortion is described by  
 167 its displacement field, written in polar coordinate, as follows [15]:

$$168 \mathbf{R}_{\text{edge}} = \frac{b}{2\pi} \left[ \beta + \frac{\sin 2\beta}{2(1-\nu)} \right] + \frac{b \times \mathbf{u}}{2\pi} \left[ \frac{1-2\nu}{2(1-\nu)} \ln|r| + \frac{\cos 2\beta}{4(1-\nu)} \right] \quad (9)$$

169  $\nu$  is the Poisson's ratio,  $\mathbf{u}$  is the dislocation line direction and  $r$  is the polar coordinate. Where  $\beta$   
 170 and  $r$  are given by:

$$172 \beta = \tan^{-1} \left( \frac{z-z_D}{x} \right) \text{ and } r = \frac{x}{\cos \beta} \quad (10)$$

173 From equations (9) and (10),  $\mathbf{R}_{\text{edge}}$  can be expressed as a function of the distance  $x$  away from the  
 174 dislocation. The new deviation parameter  $s'$  is then:

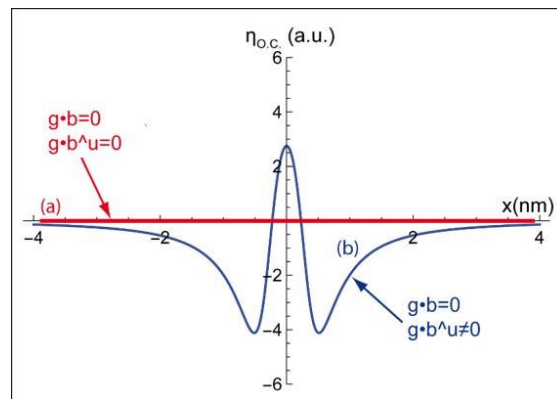
$$175 s' = s + \mathbf{g} \cdot \frac{d\mathbf{R}_{\text{edge}}}{dz} \Big|_{z=z_D} \quad (11)$$

176  
 177 The presence of an edge dislocation in the crystal can also be highlighted, analytically, by the  
 178 insertion of equation (11) in equation (5). Hence the calculated theoretical profiles are similar to that  
 179 obtained for a screw dislocation. For the diffraction  $+g$ , at Bragg condition ( $s=0$ ), the modeled curves  
 180 are characterized by a maximum and a minimum of I<sub>BSE</sub>. The edge dislocation generates, then, a  
 181 white/black contrast. However, for  $s>0$ , profile presents only a single peak consistent with  
 182 experimental observations. This maximum of intensity is situated at a position  $x \approx -6 \text{ nm}$  away from  
 183 the dislocation core. Concerning the case of  $s<0$ , the I<sub>BSE</sub> profile show a hollow with a slight peak. All

184 profiles are also reversed, following the inversion of the  $\mathbf{g}$  sign regardless of the deviation  
 185 parameter  $s$ .  
 186

### 187 2.3. Extinction criteria

188 Furthermore, for both screw and edge dislocations, considering the extinction criteria  $\mathbf{g}\cdot\mathbf{b}=0$  and  
 189  $\mathbf{g}\cdot\mathbf{b}\times\mathbf{u}=0$  in our equation leads to a null BSE yield ( $\eta_{0,c}=0$  a.u in Figure 4a). Regarding the edge  
 190 dislocation, the  $\mathbf{b}\times\mathbf{u}$  term in equation (9) becomes null when  $z=z_D$ . Nevertheless, the position of the  
 191 dislocation is located in the  $[z_1, z_2]$  range (see Figure 1), therefore the  $\mathbf{b}\times\mathbf{u}$  term is not null. For  $\mathbf{g}\cdot\mathbf{b}=0$   
 192 and  $\mathbf{g}\cdot\mathbf{b}\times\mathbf{u}\neq 0$ , in the  $[z_1, z_2]$  range except  $z_D$ , the calculated profile for an edge dislocation displays a  
 193 low intensity peak  $\eta_{0,c}\approx 2,7$  (a.u with respect to the background level) surrounded by two hollows.  
 194 Such residual contrast (Figure 4b) is characteristic of an edge dislocation observed by TEM under  
 195 these diffraction conditions [17].



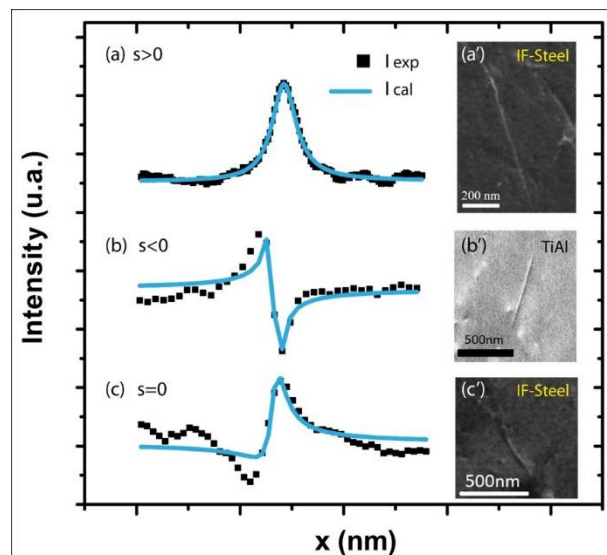
196

197 **Figure 4.**  $I_{BSE}$  profiles modeled for the extinction conditions: (a)  $\mathbf{g}\cdot\mathbf{b}=0$ ,  $\mathbf{g}\cdot\mathbf{b}\times\mathbf{u}=0$  and (b)  $\mathbf{g}\cdot\mathbf{b}=0$ ,  $\mathbf{g}\cdot\mathbf{b}\times\mathbf{u}\neq 0$ .

198

### 199 2.4. Quantitative comparisons with experimental profiles

200 In this part, for each deviation parameter:  $s>0$ ,  $s<0$  and  $s=0$ , an average profile is calculated from 50  
 201 experimental dislocation profiles and fitted by equation (5). The results are illustrated by Figures 5a,  
 202 b and c respectively.



203



204 **Figure 5.** Fitted (blue line) and experimental (black squares)  $I_{BSE}$  profiles and their corresponding ECC  
 205 micrograph obtained for (a, a')  $s>0$ , (b, b')  $s<0$  and (c, c')  $s=0$  respectively.

206 As can be seen, the best fits are obtained for  $s>0$  (the correlation coefficient  $\chi^2=2$ ) and  $s<0$  ( $\chi^2=8.7$ ).  
 207 While for  $s=0$ , the general features of the curve are well modeled but the correlation coefficient is  
 208 higher:  $\chi^2=16.4$ . At Bragg condition because of the strong interaction between the electron beam and  
 209 the crystal atoms [18], dynamical effects are magnified and the diffracted intensity is higher enough  
 210 to excite neighboring reflections. Then the successively and coherently produced beams interfere  
 211 with each other. The "n" beam approach must thus be considered to better report the experimental  
 212 results. Besides, in our calculations multiple scattering was treated incoherently.

213 Nevertheless, the fitted profiles provide, among other parameters, reasonable orders of magnitude  
 214 of the physical parameters  $\xi_g$ ,  $\xi_0'$  and  $\xi_g'$  for different deviation parameters and materials (IF-steel:  
 215 Figure 5a, a', c and c' TiAl: Figures 5b and b'). Furthermore, the obtained parameters are in good  
 216 agreement with the values reported in the literature [11]. Such as the case of IF-steel:  $\xi_g=9,4\pm 1,3$  nm ;

217  $\xi_0'=170,4\pm 36,7$  nm ;  $\xi_g'=177,7\pm 38,3$  nm.

### 218 3. Conclusions

219 In this paper an original theoretical model based on the Bloch wave approach of the dynamical  
 220 diffraction theory was developed for modeling  $I_{BSE}$  around dislocations without resorting to  
 221 numerical methods. An analytical formula of the BSE signal as a function of the different physical  
 222 parameters governing the ECCI experiment is proposed for the first time to our knowledge. The BSE  
 223 contrast profiles, produced by screw and edge dislocations parallel to the sample surface, display the  
 224 same appearance for the diffraction conditions. For a deviation parameter  $s=0$  (Bragg condition) and  
 225  $s<0$ , the theoretical BSE curves show hollow and peak of intensity corresponding to the black and  
 226 white dislocation sides respectively. The inversion of the  $\mathbf{g}$  leads to the profile inversion (hollow  
 227 becomes peak and vice versa). For  $s>0$ , the bright dislocation contrast is envisaged in the modeled  
 228 profile by the intensity peak. This latter (dislocation image) do not coincide with the exact  
 229 dislocation position ( $x=0$ ) and it is displaced to the opposite side when the  $\mathbf{g}$  is reversed. Moreover,  
 230 our theoretical model confirms the use of the invisibility criteria in ECCI.

231 The good agreement between the theoretical and experimental results was also confirmed by  
 232 adjusting the BSE intensity profiles. Hence, deduced values for the physical parameters  $\xi_g$ , the  
 233 extinction distance and  $\xi_0'$  and  $\xi_g'$ , the absorption lengths are consistent with the literature.

234 Because the use of ECCI is becoming widespread for the defects characterization in bulk material in  
 235 SEM, we provide a usable formula of the BSE intensity produced by dislocations. Furthermore, our  
 236 approach can be extended to other defects. Now ECCI is mature for exploring new horizons in  
 237 Materials Science.

238

239 **Author Contributions:** All ECCI observations were performed by H.K. H.K., A.G. and N.M. performed the  
 240 theoretical interpretations. H.K. wrote the main manuscript text. All the authors participate in the discussion.



241 **Conflicts of Interest:** The authors declare no conflict of interest.

## 242 **References**

- 243 1. Booker, G. R.; Shaw, A. M. B.; Whelan, M. J.; Hirsch, P. B. Some comments on the interpretation of the  
244 Kikuchi-like reflection patterns observed by scanning electron microscopy. *Phil. Mag.* **1967**, *16*, 1185-1191.
- 245 2. Mansour, H.; Guyon, J.; Crimp, M. A.; Gey, N.; Beausir, B.; Maloufi, N. Accurate electron channeling  
246 contrast analysis of dislocations in fine grained bulk materials. *Scripta. Mater.* **2014**, *84-85*, 11-14.
- 247 3. Kriaa, H.; Guitton, A.; Maloufi, N. Fundamental and experimental aspects of diffraction for  
248 characterizing dislocations by electron channeling contrast imaging in scanning electron microscope. *Sci.*  
249 *Rep.* **2017**, *7*, 9742.
- 250 4. Howie, A.; Whelan, M. J. Diffraction contrast of electron microscope images of crystal lattice defects. II.  
251 The development of a dynamical theory. *Proc. Royal. Soc.* **1961**, *263*, 217-237.
- 252 5. Howie, A.; Whelan, M. J. Diffraction contrast of electron microscope images of crystal lattice defects. III.  
253 Results and experimental confirmation of the dynamical theory of dislocation image contrast. *Proc.*  
254 *Royal. Soc.* **1962**, *267*, 206-230.
- 255 6. Wilkinson, A. J.; Hirsch, P. B. Electron diffraction based techniques in scanning electron microscopy of  
256 bulk materials. *Micron.* **1997**, *28*, 279-308.
- 257 7. Spencer, J. P.; Humphreys, C. J.; Hirsch, P. B. A dynamical theory for the contrast of perfect and imperfect  
258 crystals in the scanning electron microscope using backscattered electrons. *Phil Mag.* **1972**, *26:1*, 193-213.
- 259 8. Wilkinson, A. J.; Hirsch, P. B.; Czernuszka, J. T.; Long, N. J. Electron channeling contrast imaging of  
260 defects in semi-conductors. *Proc. Micros. Semiconduct. Mater.* **1993**, *134*, 755-762.
- 261 9. Wilkinson, A. J.; Hirsch, P. B. The effects of surface stress relaxation on electron channelling contrast  
262 images of dislocations. *Phil. Mag. A.* **1995**, *72:1*, 81-103.
- 263 10. Reimer, L.; Heilers, U.; Saliger, G. Kikuchi band contrast in diffraction patterns recorded by transmitted  
264 and backscattered electrons. *Scanning.* **1986**, *8*, 101-118.
- 265 11. Reimer, L. *Scanning Electron Microscopy. Physics of image formation and microanalysis.*  
266 Springer-Verlag Berlin Heidelberg GmbH, 2nd edition (**1998**).
- 267 12. Zeafferer, S.; Elhami, N. N. Theory and application of electron channelling contrast imaging under  
268 controlled diffraction conditions. *Acta. Mat.* **2014**, *75*, 20-50.
- 269 13. Clarke, D. R.; Howie, A. Calculations of lattice defect images for scanning electron microscopy. *Phil. Mag.*  
270 **1971**, *24* (190), 959-971.
- 271 14. Cockayne, D. J. H.; Ray, I. L. F.; Whelan, M. J. Investigations of dislocation strain fields using weak beams.  
272 *Phil. Mag.* **1969**, *20-168*, 1265-1270.
- 273 15. Hirth, J. P.; Lothe, J. *Theory of dislocations.* A Wiley-Interscience Publication, 2nd edition (**1982**).
- 274 16. Guitton, A. Joulain, A. Thilly, L. Tromas, C. Dislocation analysis of Ti2AlN deformed at room  
275 temperature under confining pressure. *Sci. Rep.* **2014**, *4* (6358), 1-4.
- 276 17. Edington, J. W. *Interpretation of Transmission Electron Micrographs.* London (**1976**).
- 277 18. Williams, D.B.; Carter, C. *Transmission Electron Microscopy.* Springer, New York (**1996**).

279